Investigation of Pulse-Reverse Electrodeposited Copper Electrocatalysts for Carbon Dioxide Reduction to Ethylene

Sujat Sen[a], Brian Skinn[b], Rajeswaran Radhakrishnan[b], McLain Leonard[a], and Fikile R. Brushett[a, *]

[a] Department of Chemical Engineering, Massachusetts Institute of Technology, Cambridge, MA 02139, USA, [*]E-mail: brushett@mit.edu
[b] Faraday Technology, Inc., Englewood, OH 45315, USA

This paper discusses the electrodeposition of thin copper (Cu) films on stainless steel substrates using pulse-reverse waveforms and the suitability of such films for electrocatalytic conversion of carbon dioxide (CO_2) to hydrocarbon products such as methane and ethylene. Activation of these Cu layers through thermal oxidation and subsequent electrochemical reduction is also explored as a means of tuning selectivity toward higher hydrocarbons. An appreciable benefit in terms of overall hydrocarbon selectivity versus hydrogen evolution and other undesirable side reactions was observed from the use of pulsed methods, and the use of thermal activation resulted in a strong shift in the hydrocarbon product distribution from methane to ethylene.

Introduction

Carbon dioxide (CO_2) emissions from base-load power plants present an entry point for recycling of the carbon in flue gas by conversion to energy-dense fuels and/or high-value chemicals. Such conversion technologies have the potential to reduce dependence on limited fossil fuel resources and to mitigate losses in overall fuel efficiency (e.g., due to vented steam) during periods of off-peak electricity demand. Copper (Cu) is well known as a unique catalyst for the electrochemical CO_2 reduction reaction (eCO_2RR), capable of forming alcohol (e.g., ethanol) and hydrocarbon (e.g., methane (CH_4), ethylene (C_2H_4)) products in addition to aldehydes, carboxylic acids, and carbon monoxide (CO) (1, 2). Ethylene is of specific interest as its role as a platform feedstock for the chemicals and plastics industries affords an appreciably higher market value than many other potential products (3). However, to date, the performance achieved with Cu catalysts and CO_2-saturated aqueous carbonate solutions have not been sufficient to enable development of an industrially viable process. Furthermore, the microstructure of metallic catalysts is known to influence various properties including selectivity and activity and, for Cu in particular, crystallographic orientation has been reported to have a strong effect on the selectivity for C_2H_4 versus CH_4 (4, 5). Given that pulsed electrodeposition is known to have a significant effect on the microstructure of the resulting metal films (6, 7), this fabrication approach may offer pathways to novel, high performance Cu catalysts for eCO_2RR.

In conventional direct current (DC) electrodeposition, a constant current (galvanostatic, more common) or constant potential (potentiostatic, less common) is applied for the duration of the process, and control is maintained through the addition of a complex mixture of additives ("levelers," "suppressors," "brighteners," etc.). By

interrupting this constant current/potential, as in pulsed methods, one may achieve results not possible with conventional DC techniques while simultaneously eliminating costly and often unstable additive chemistries (8). Properties that can be adjusted/enhanced with appropriate tuning of the pulsed electrodeposition waveform include nucleation density, microstructure (e.g., grain size), and residual stresses as well as macroscopic deposit uniformity. Further, in alloy electrodeposition applications, adjustment of the pulse waveform can also enable control over the composition of the deposited material (9, 10). Pulse and pulse-reverse processes enable these capabilities due to the nearly unlimited combinations of peak current densities, duty cycles, and frequencies that can be employed, enabling precise control of the mass transfer and surface reactions during electrodeposition (8, 11).

In this work, we investigate the use of pulse-reverse electrodeposition methods as a means to fabricate Cu catalyst layers on stainless steel substrates for eCO_2RR with a focus on gaseous hydrocarbon production. The role of electrodeposition conditions as well as post-deposition activation protocols (here, thermal oxidation followed by electrochemical reduction) are characterized through electrochemical analysis, scanning electron microscopy, and X-ray diffraction. In combination, these techniques enable the development of preliminary structure-performance relations which can be used to guide future development efforts.

Experimental

Materials

High purity potassium carbonate (99.99%, Sigma Aldrich, St. Louis, MO, USA), Sodium carbonate (99.5%, Sigma), sodium sulfate (99%, Sigma), ethyl viologen dibromide (99%, Sigma), hydrochloric acid (37%, Sigma), Cu foil (99.9%, Goodfellow Corp., Coraopolis, PA, USA), copper sulfate (> 98%, Sigma), sulfuric acid (95-98%, Chemical Services, Inc., Dayton, OH, USA), poly(ethylene glycol) (PEG, Sigma), and CO_2 (99.99%, Research Grade 5.0, Airgas, Dorchester, MA) were used as received. Stainless steel sheets (SS304, 4 in. × 4 in. × 0.018 in., Online Metals, Seattle, WA, USA) were used as substrates/panels. A mixed metal oxide (MMO) anode (Republic Anode, Valley City, OH, USA) was used as the counter electrode for activation/reduction of Cu catalyst layer. Alumina blast powder (80-grit, Midvale Industries, Inc.) was used to roughen the substrate surface before plating. Plated substrates were sectioned using alumina cutting wheels in an Accutom-5 cutoff saw (Struers, Inc., Cleveland, OH, USA).

Electrodeposition of Cu onto Stainless Steel Panels

Cu catalyst electrodeposition was carried out in a retrofitted custom electrochemical cell, similar to that described previously (12). The cell was charged with Cu electrodeposition electrolyte, composed of copper (II) sulfate, sulfuric acid, chloride ion (as hydrochloric acid), and poly(ethylene glycol) dissolved in deionized water. The SS304 panels were cleaned with acetone, dry blasted with 80 grit alumina, cleaned with deionized water, and dried with a stream of compressed air before being mounted in the cell. Cu was deposited onto the panels at uncontrolled ambient temperature (ca. 25 °C) using DC or pulse-reverse waveforms under current control for a predefined period of time. The actual voltage and current responses in the cell were measured using an

oscilloscope (Tektronix, Salem, OR, USA) to confirm the fidelity of the applied waveform and to calculate the actual net cathodic charge passed in each test. Both pulsed and DC electrodeposition protocols were conducted to a constant net cathodic charge density of 20 C/cm^2. After plating, the Cu-coated steel panels were removed from the cell, rinsed under a gentle stream of deionized water, photographed, and left to air dry overnight at room temperature. The dried panels were sectioned into coupons (50 mm × 26 mm) sized to fit the electrochemical testing cell (*vide infra*).

Activation and Oxide-Reduction of Cu Catalyst Layer

The Cu-plated coupons were subjected to an activation protocol modified from that of Li and Kanan (13), by thermal oxidation in air in a muffle furnace (48000 Furnace, Barnstead/Thermolyne Corp., Dubuque, IA, USA). The specific heating profile used was:

1. Heat from room temperature to 110 °C at 3 °C/min
2. Dwell at 110 °C for 1 h
3. Heat to T_{peak} at 3-9 °C/min
4. Dwell for a set time at T_{peak}
5. Cool to room temperature at a maximum rate of 2 °C/min

The peak activation temperature (T_{peak}) was typically no greater than 350 °C, as listed in Table 1, due to failures in film adhesion observed from activation at higher temperatures. After activation, the samples were electrochemically reduced in a cell containing CO_2-saturated aqueous 0.1 M Na_2CO_3. The coupons were mounted in parallel as cathodes against a MMO counter electrode in a two-electrode configuration. An initial cathodic potential of -400 to -500 mV was applied, followed by cathodic potential steps of -100 mV with dwell times of 1 min at each potential. The reduction procedure was terminated when visible gas evolution was observed at the coupons, typically ca. -1900 mV. This was accompanied by the onset of a color change of the oxidized films from black/gray (Cu oxide) to brown/red (Cu). Photographs of a representative part at the various stages of processing are shown in Figure 1.
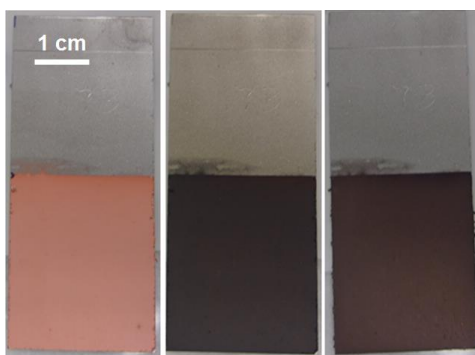

Figure 1. Various stages of electrodeposition (left), activation (center), and reduction (right) of a representative Cu catalyst layer on a stainless steel substrate.

Electrocatalysis Experiments and Performance Evaluation

A small volume custom cell was used for all electrochemical testing in this study based on a configuration described by Kuhl et al. (14) (Figure 2). The cell body (i.e.,

backing plates, anolyte/catholyte chambers) was machined from acrylic (Optically Clear Cast Acrylic Sheet, ½ in. thick, 6 in. × 12 in., McMaster, Princeton, NJ) using a CNC mill (Roland DG Corporation, Model AProII, Rotary Axis Unit, ZCL-540). The cell was sealed with Norprene rubber gaskets (McMaster). The assembled cells had geometric cathodic area of 0.25 cm^2 defined by masking with Kapton tape (McMaster). A MMO anode was used as the counter electrode (3 cm × 1.5 cm) and Selemion anion exchange membrane (AEM, Asahi Glass Engineering Co., Ltd.) was used to separate the anolyte and catholyte chambers. Typical volumes of the catholyte and anolyte were ca. 6 mL and ca. 10 mL respectively. All experiments were conducted potentiostatically against a Ag/AgCl electrode (+197 mV vs. SHE, BASi Inc., West Lafayette, IN) positioned in front of the working electrode (< 0.5 cm), which was calibrated against a saturated calomel electrode (+242 mV vs. SHE, Fisher Scientific) prior to each run. The cathode-to-anode distance was fixed at ca. 1 in. Electrolyte solutions were prepared using conductivity grade deionized water. Electrolysis was performed using an aqueous solution of CO_2-saturated 0.1 M K_2CO_3 under potentiostatic conditions using a VSP-300 Biologic multichannel potentiostat with 85% iR correction. CO_2 was delivered to both cell compartments at a constant flow rate of 10 mL/min for 30 min prior to electrolysis to saturate the solution and maintained throughout the experiment. Cyclic voltammetry experiments were performed in the same cell, prior to conducting electrolysis. Currents reported throughout the manuscript are normalized to the geometric area of the electrode to obtain current densities (mA/cm^2).
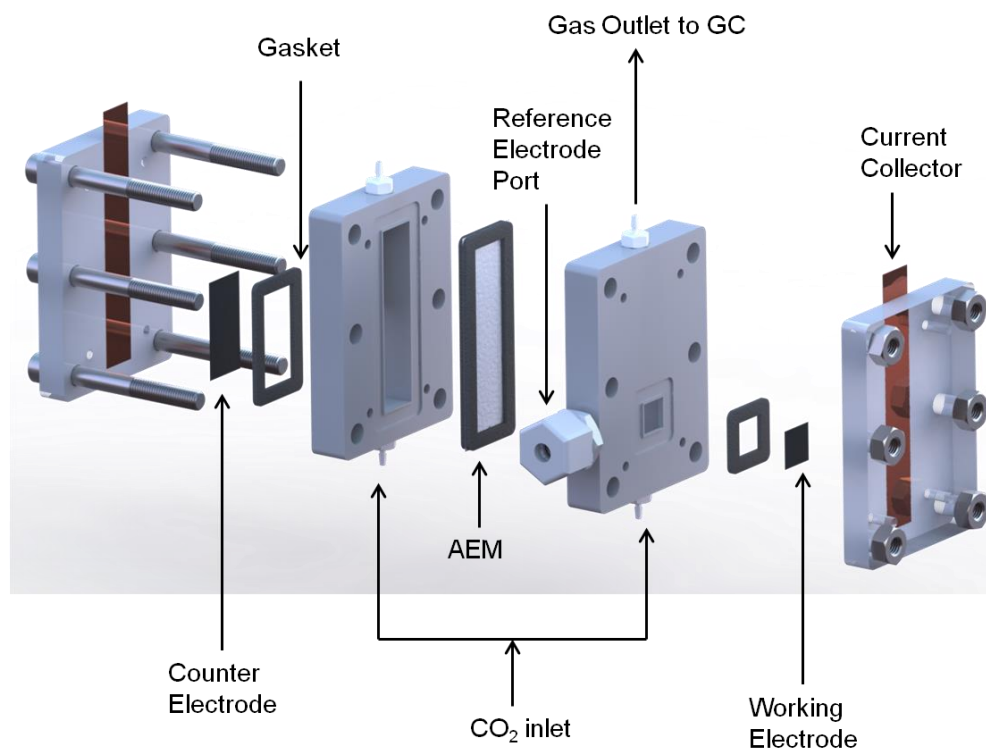

Figure 2. Exploded view of a three-dimensional CAD rendering of reactor used for electrochemical experiments.

Product Quantification

Gaseous products in the effluent gas stream from the cathodic half of the cell were measured by injecting an aliquot of the effluent gas stream via an automated sample loop into a gas chromatograph (GC, Agilent 7890). Current efficiencies (CEs) of each product were determined from the measured product concentration divided by the theoretical maximum concentration calculated from the number of coulombs passed during electrolysis. As our focus is only on gaseous CO_2 reduction products, we did not quantify liquid phase products, and while the CEs for hydrogen evolution were measured, they are omitted below. Across the range of experimental conditions tested, the hydrogen evolution CEs were 60-90%. Typically, electrolysis was performed for 1-2 h, and the values of CE reported are the average of values derived from 3-4 GC measurements taken periodically during electrolysis (typically, at 12 min intervals starting at 5 min after initiating electrolysis). For all these measurements, the product concentrations were found to be stable within $\pm$ 5%.

Ex-Situ Analyses

Scanning electron microscope (SEM) images were acquired using a Zeiss Merlin High Resolution SEM without the use of any conductive coating. X-ray diffractograms (XRD) were obtained using a Rigaku Smartlab instrument with Cu K-α radiation in Bragg-Brentano geometry working at 200 mA and 45 kV. XRD were obtained in the 2θ range of 20° to 100°, with steps of 0.02° and acquisition times of 0.1 s per step.

Results and Discussion

Electrodeposition and Activation of Cu

Figure 3 illustrates three pulse waveforms explored in this study, H, M, and L, with variable magnitudes (high, medium, and low) of forward (cathodic) peak current density but equal reverse (anodic) peak current density and duration. All three waveforms were defined such that the forward (cathodic) portion of the pulse represented delivery of an equal number of coulombs per unit area, per pulse cycle. Accordingly, the net cathodic charge delivered per unit area, per pulse cycle, was also equal for all three waveforms. Waveform M also incorporated an off-time between the cathodic and anodic pulses. DC electrodeposition was performed for comparison using a constant current density of 17 mA/cm^2. When activated with the original protocol described by Kanan and co-workers (13) (T_{peak} = 500 °C), the adhesion of the formed black/gray oxide film was generally poor, spalling readily to reveal un-oxidized Cu underneath. Thus, all samples were activated at temperatures $T_{peak} \leq 350$ °C where the formed oxide films were mechanically stable. The electrodeposition method and thermal activation conditions for the various samples explored in this study are shown in Table 1. Assuming 100% cathodic and anodic current efficiency for copper deposition and removal, respectively, the 20 C/cm^2 net passed cathodic charge on the samples yields a typical Cu layer thickness of ca. 15 μm.
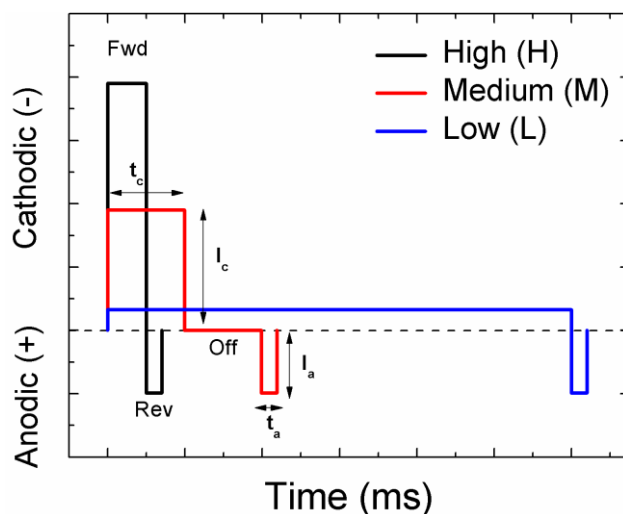
Figure 3. Pulse waveforms H, M, and L used for the electrodeposition of Cu with identical backward (anodic) pulse, varying magnitudes of forward (cathodic) pulse, but with equivalent net cathodic charge passed per cycle. The variables t_i and I_i represent the duration and magnitude of a given pulse within each waveform, where the subscripts 'c' and 'a' indicate the cathodic and anodic pulses, respectively.

Measurement of Electrochemically Accessible Surface Area

   Cyclic voltammetry (CV) in the presence of a known ethyl viologen (EV) dibromide concentration was used to estimate the accessible electro-active surface area of various electrodeposited samples normalized to a commercial Cu plate electrode (mechanically polished with 400 grit sandpaper) of unit geometric area (1 cm^2). A plot of peak current as a function of the square root of scan rate for all samples was found to be linear, confirming the electrochemical process to be diffusion-limited and enabling the use of the Randles-Sevcik equation to estimate the electro-active surface area (15). Only the first electron transfer event, from EV^{2+} to EV^+, was accessed from which the diffusion coefficient (D_0) of ethyl viologen dibromide was determined to be 1.6×10^{-8} cm^2/s, which is comparable to prior reports (16). Using this diffusion coefficient, the Randles-Sevcik equation was then used to estimate electrochemically accessible surface area for all samples (see Table 1). All values are normalized to the geometric area of the Cu plate.

TABLE 1. Deposition protocol, activation conditions, grain size, and relative electrochemically active surface area for the samples reported in this study. Samples with no T_{peak} value indicated were tested in the as-deposited condition.

Sample ID	Electrodeposition Waveform	T_{peak} (°C)	Grain Size (nm)	Relative Electro-Active Surface Area
Cu (commercial)	-	-	-	1.00
#5F	Pulsed H	350	41	1.85
#10E	DC	350	42	5.71
#10F	DC	-	27	2.37
#13E	Pulsed L	350	37	4.69
#13F	Pulsed L	-	35	1.08
#15B	Pulsed L	300	76	4.41
#18A	Pulsed M	350	91	4.21

XRD Characterization

Typical XRD of as-plated and thermally activated Cu samples are shown in Figure 4 for both DC and pulse-plated samples. No major impurity peaks were observed. Database (ICSD) standards for polycrystalline (fcc) Cu and Cu(I) oxide are also included for comparison. The presence of polycrystalline (fcc) Cu in both the as-plated and activated samples was confirmed. Furthermore, Figures 4(a) and 4(b) (top traces) show small but discernible diffraction peaks at ca. 37° and ca. 62° for both activated samples (#10E and #13E), indicated by arrows. These are attributed to the presence of an oxide layer. Note that no oxide peaks are visible in the as-plated samples (#10F and #13F). The crystallite sizes were calculated using Scherrer's formula for the peak at ca. 50°, assuming spherical particle morphology, and are reported in Table 1.
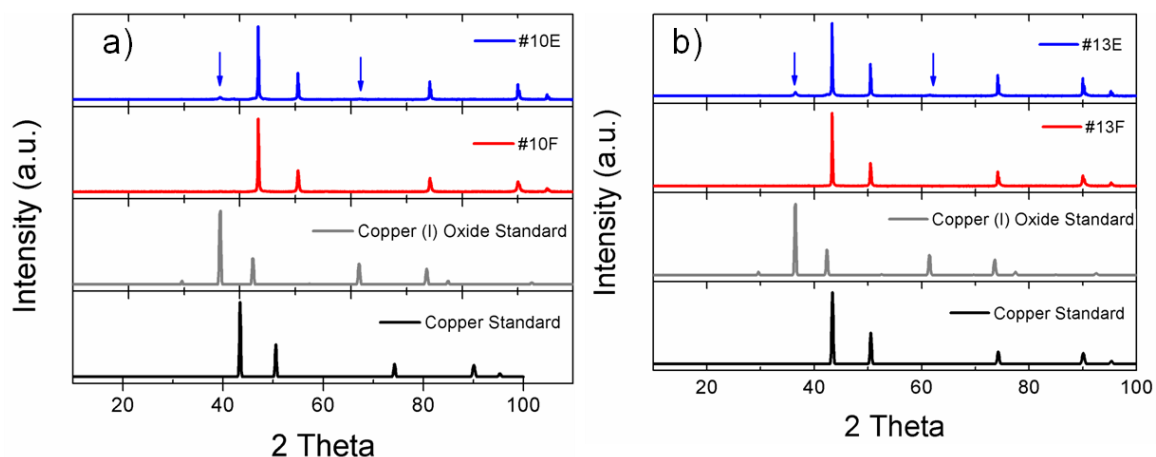

Figure 4. XRD patterns of (a) DC-plated samples before (#10F) and after (#10E) activation at 350 °C and (b) pulse-plated samples before (#13F) and after (#13E) activation at 350 °C. For comparison, ICSD standards for Cu metal and Cu(I) oxide are included.

SEM Analysis

Figure 5 shows the SEM images of Samples #10F (a, b) and #10E (c, d), which were both electrodeposited using the DC protocol, but with the latter activated at 350 °C following electrodeposition. The as-plated Sample #10F shows no distinct features at low magnification but has a clear fine structure consisting of discrete particles that are less than 1 μm. In contrast, the activated Sample #10E shows several cracks at low magnification, which is likely a side effect of the thermal treatment. Specifically, oxidation of any residual carbon (e.g., PEG from the electrodeposition bath) during the activation step could lead to evolution of CO_2 resulting in partial cracks in the Cu film. Higher magnification shows this sample also consists of particles of sizes much less than 1 μm, but fused together, likely due to a sintering process (17) during activation at 350 °C. Based on CV measurements (Table 1), the ratio of electroactive areas between the two samples is 2.4 (#10E / #10F), which is qualitatively consistent with the SEM observations of fine structure.
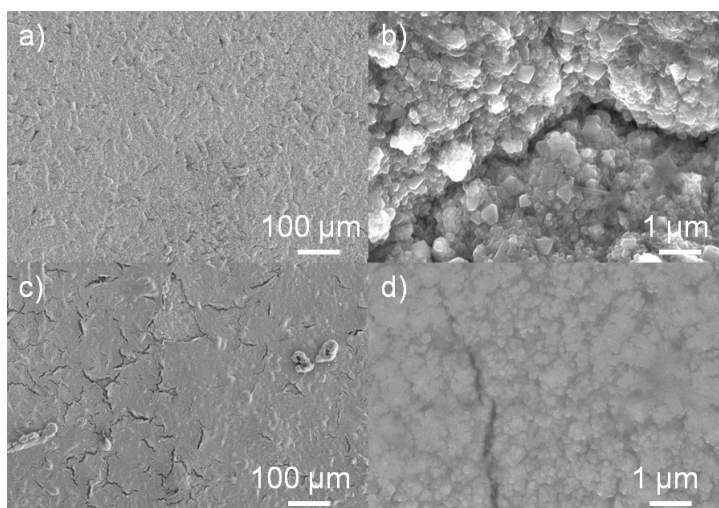
Figure 5. SEM images of DC-plated Cu on steel: (a, b) as-plated Sample #10F and (c, d) activated Sample #10E.

Figure 6 shows the SEM images of Samples #13F (a, b) and #13E (c, d), which were both electrodeposited using the pulsed waveform with a low-intensity forward pulse (Pulsed L, Table 1), with the latter activated at 350 °C following electrodeposition. The as-plated Sample #13F does not show distinct features at low magnification, but has a clear fine structure consisting of discrete particles in the 2-10 μm range. No sub-micron features were visible. Note that this is in contrast to the as-plated DC Sample #10F, (Figure 5(a) and 5(b)), which exhibited a much smaller fine structure (< 1 μm).
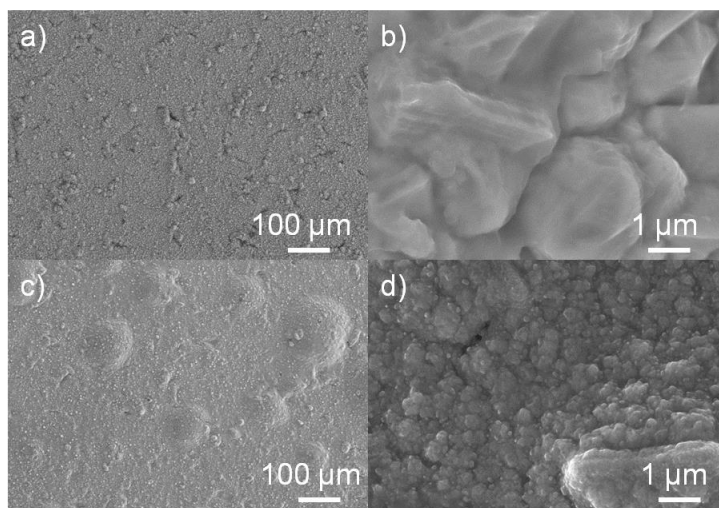

Figure 6. SEM images of pulse-plated Cu on steel (a, b) as-plated Sample #13F and (c, d) activated Sample #13E.

The activated Sample #13E shows several cracks at low magnification, as well as protrusions likely due to the thermal treatment. As mentioned above, oxidation of any residual carbon could lead to evolution of CO_2, resulting in the observed partial delamination of the Cu from the steel substrate. Higher magnification also shows a fused structure with particle sizes less than 1 μm, presumably arising from the breakdown of the micron sized aggregates observed before activation (Figure 6(b)). Based on the data

of Table 1, the ratio of electroactive areas is 4.3 (#13E / #13F), which is again qualitatively consistent with the SEM observations of fine structure developed during activation.

Effect of Forward Pulse Shape

As noted, three pulsed electrodeposition waveforms were used in this study (H, M, and L), which differed primarily in the intensity of the forward (cathodic) portion of each waveform. A high magnitude, short duration forward pulse (i.e., as with waveforms H and M) creates a large driving force for Cu electrodeposition on the steel substrate surface, typically leading to the formation of a large number of nucleation sites. This is in contrast to pulse waveform L, which applies a tenfold longer, but also tenfold lower magnitude forward pulse, which usually allows for sustained Cu growth on the steel surface from a more limited number of nucleation sites.

With increasing forward peak current, the post-activation sub-micron fine structure becomes more distinct (Figure 7), with Sample #5F (Pulsed H) exhibiting a discrete nanostructure comprising of 400-500 nm cubes. In comparison, Sample #13E (Pulsed L), electrodeposited at lower forward peak current, exhibits a less discernible and more fused sub-micron structure. Consistent with this trend, Sample #18A (Pulsed M) exhibits an intermediate fine structure with partially fused 100-200 nm particles. Based on the data of Table 1, the electroactive area of these electrodes were found to be in the order of #5F < #18A < #13E, which suggests that the smaller particle size visible in the SEM images correlates well with active surface area.
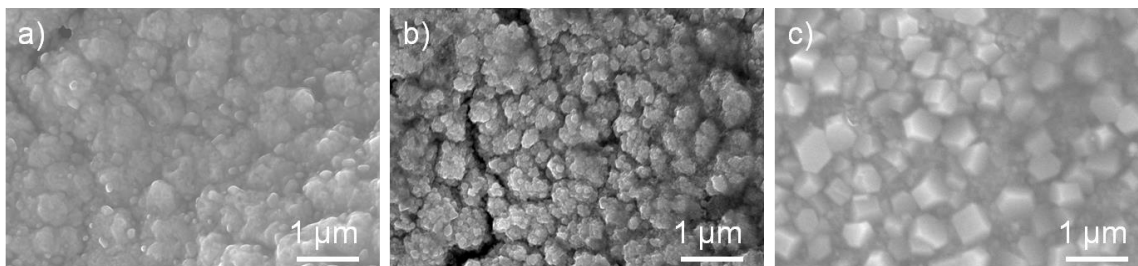

Figure 7. SEM images of Samples (a) #13E (Pulsed L), (b) #18A (Pulsed M), and (c) #5F (Pulsed H), electrodeposited using pulse waveforms of successively increasing forward peak current as described in Figure 3(a). All samples were activated at 350 °C prior to imaging.

While the precise mechanisms underlying these variations in morphology are not fully understood, it is hypothesized that they arise from differences in the residual stresses within the deposited films. Metallic deposits prepared with more "DC-like" waveforms (longer, lower intensity forward pulses, as in Pulsed L) tend to exhibit tensile residual stresses (18-20). It is possible that these stresses lead to dendritic surface transformations at the elevated temperatures of the activation protocol. Conversely, the residual stresses of deposits fabricated with high amplitude, short duration cathodic pulses tend to be minimal, or even compressive in nature, potentially leading to less dendritic (more consolidated) morphology after thermal treatment. The above trends in surface morphology and active area discussed for Figure 7 appear consistent with this model.
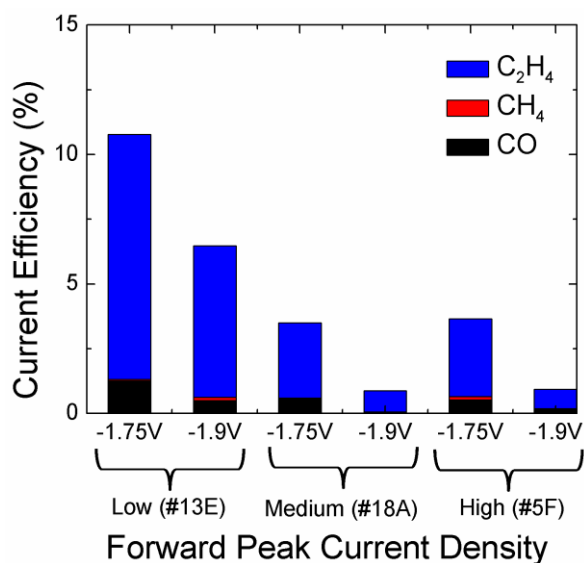
Figure 8. Current efficiency at two applied potentials (vs. Ag/AgCl) during eCO$_2$RR experiment, plotted as a function of forward peak current applied during the electrodeposition pulse sequence (see Figure 3).

Figure 8 shows the CEs of the gaseous products detected for eCO$_2$RR (i.e., CO, CH$_4$, and C$_2$H$_4$) for the three samples (#13E, #18A, and #5F), from hour-long electrolysis experiments. An inverse correlation is observed between forward peak current and CE for C$_2$H$_4$ formation at both electrolysis potentials. Given the relative trends in surface area measurements (Table 1) and fine structure seen in Figure 7, C$_2$H$_4$ production appears to be increasingly favorable on the surfaces with finer structure, consistent with prior literature (21-23).
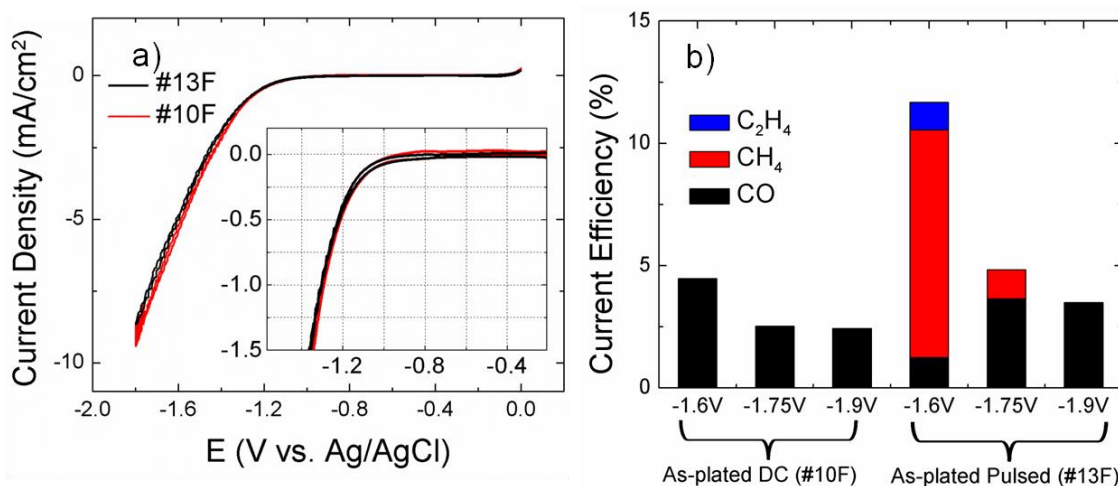
Electrocatalysis – As-Plated Samples

Figure 9. (a) Stabilized CVs of Samples #10F (as-plated, DC) and #13F (as-plated, pulsed); (b) Plot of CE for the same samples at various applied potentials (vs. Ag/AgCl) during eCO$_2$RR experiments.

Figure 9(a) shows the CVs of two samples electrodeposited using a DC (#10F) and pulsed (#13F) protocol, both without activation. Both samples exhibit a similar onset

potential (see inset) of ca. -1.3 V, which is close to the typical literature value of ca. -1.2 V reported for polycrystalline Cu under similar conditions (15). Figure 9(b) shows the CE of the gaseous products of eCO$_2$RR (i.e., CO, CH$_4$, and C$_2$H$_4$) for the same samples, from electrolysis experiments. As-plated Sample #10F generates CO at all potentials, with little to no detectable CH$_4$ or C$_2$H$_4$. Though not shown, electrolysis potentials higher than -1.9 V were also explored, but yielded no appreciable hydrocarbon products. Note that this is in contrast to the behavior of polycrystalline Cu, which is reported to generate ca. 25% CH$_4$ and 40% C$_2$H$_4$ at -1.0 V vs. RHE (-1.6 V vs. Ag/AgCl) (13). In comparison, the as-plated sample obtained with a pulsed waveform (#13F) shows all three eCO$_2$RR products of interest at -1.6 V, with ca. 9% CH$_4$ production. Higher potentials shift selectivity back to CO and H$_2$ production. Note that the electroactive area per unit geometric area is larger for the DC-plated sample (#10F / #13F ≈ 2.1, Table 1), consistent with the SEM fine structure seen in Figures 5(b) and 6(b), respectively. However the magnitudes of the cathodic current for these two samples seen in Figure 9(a) do not differ considerably, suggesting other factors such as surface texture and associated mass transport limitations (24) are affecting the eCO$_2$RR current density.

Electrocatalysis – Activated Samples

Figure 10(a) shows the CVs of two samples electrodeposited using a DC (#10E) and pulsed (#13E) protocol, both activated at 350 °C. A distinct capacitive contribution is now visible in both samples (cf. Figure 9), indicative of increased surface roughness, presumably due to the activation process and consistent with active area measurements (Table 1).
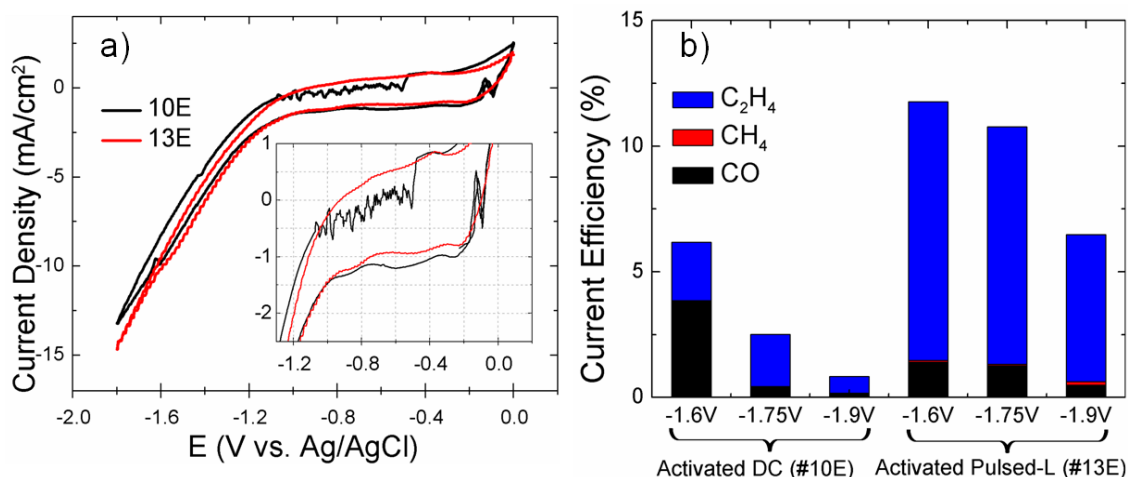

Figure 10. (a) Stabilized CVs of Samples #10E (DC plated) and #13E (pulse plated), both activated at 350 °C; (b) Plot of product CEs for the same samples at various applied potentials (vs. Ag/AgCl) during eCO$_2$RR experiments.

Both samples exhibit a similar onset potential (inset) at ca. -1.1 V, which is slightly anodic of the typical literature value of ca. -1.2 V reported for polycrystalline Cu under similar conditions (15). Note this value of -1.1 V is nearly 200 mV anodic of the same samples without activation (cf. the -1.3 V noted in Figure 9(a)), representing a significant lowering of the overpotential. This translates to an earlier (more anodic) observed

thermodynamic onset potential for the CO_2 reduction reaction, which has favorable implications for the energy efficiency of the activated catalysts.

Figure 10(b) shows the CEs of the gaseous products of eCO_2RR for the two samples, from hour-long electrolysis experiments. Sample #10E generated a mixture of C_2H_4 and CO with little to no CH_4 at all applied potentials. Electrolysis potentials more cathodic than -1.9 V were also explored, but yielded no significant differences. Sample #13E, which was activated under the same conditions, but deposited using a pulsed waveform (Pulsed L), exhibits similar selectivity for C_2H_4 and CO, forming little to no CH_4 at all potentials. However, the efficiency to C_2H_4 is observed to be higher at all potentials (vs. Sample #10E), with a maximum of ca. 10% at -1.6 V.

Electrocatalysis – Effect of Activation Temperature

Figure 11(a) shows the CVs of three samples electrodeposited under the same pulse waveform (Pulsed L), with one analyzed as-plated and the other two activated at different temperatures (300 and 350 °C). The anodic shift in onset potential (see inset) from -1.3 V (#13F) to -1.1 V (#13E, #15B) is attributed to the activation of the samples. The similar values of onset potentials for #15B and #13F indicate little or no effect of the activation temperature. However, the higher current density for Sample #15B (activated at 300°C) compared to Sample #13E (activated at 350°C) suggests a superior catalytic activity towards H^+ or CO_2 reduction even though the accessible surface area is slightly lower (#13E > #15B, Table 1).
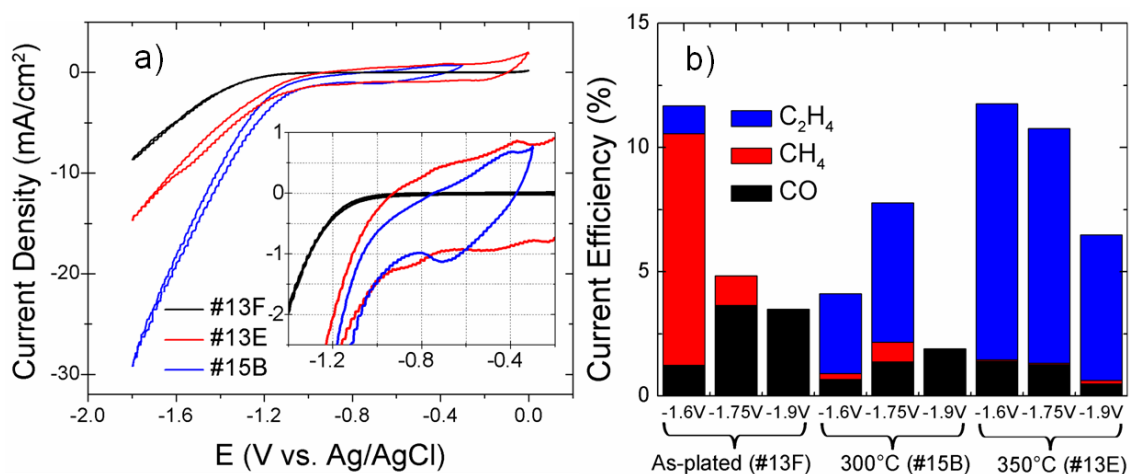

Figure 11. (a) Stabilized CVs of Samples #13F (as-plated), #15B (activated at 300 °C), and #13E (activated at 350 °C) electrodeposited using waveform Pulsed L; (b) CEs obtained from eCO_2RR experiments, plotted as a function of activation protocol for the same samples at different applied potentials (vs. Ag/AgCl).

Figure 11(b) shows the CE of the gaseous products detected for eCO_2RR for the same three samples, from hour-long electrolysis experiments. As-plated Sample #13F generates a mixture of all three products at -1.6 V, with CH_4 as major product. Negligible amounts (<< 1%) of C_2H_4 was observed at higher potentials. Upon activation at 300 °C, (Sample #15B) the product distribution profile changes dramatically to favor the production of C_2H_4, with CH_4 and CO being the minor products. Activation at even

higher temperatures (350 °C for Sample #13E) increases the selectivity to C_2H_4 even further, at all potentials explored. Typical selectivity ratio of this sample for C_2H_4 / CH_4 at -1.6 V is 172. Note that the active area per unit geometric area increases in the same order as does the selectivity for ethylene (1 : 4.08 : 4.34, #13F : #15B : #13E, Table 1). The maximum observed current efficiency for C_2H_4 production of ca. 10% is consistent with the literature-reported values of oxide derived Cu (13). The remainder of the gaseous products for Sample #13E and #15B was H_2, with average CEs of 71 and 89% respectively. The larger CE of H_2 evolution for Sample #15B suggests superior catalytic activity for H^+ reduction, as observed in the CV (Figure 11(a)).

Figure 12 shows the SEM images of these three samples, emphasizing the differences in their sub-micron structure. As discussed previously, as-plated Sample #13F shows no distinct nanostructure at low magnification but has a clear fine structure consisting of discrete particles in the 2-10 µm range. The sample activated at 350 °C (#13E) shows a fused structure with particle sizes of less than 1 µm, which appears to arise from the breakdown of the micron sized aggregates observed before activation. Sample #15B, activated at a lower temperature of 300 °C, shows a more complex fine structure consisting of both micron size aggregates (similar to #13F) and a fused nanostructure (similar to #13E). Furthermore, several voids were also observed, which depending on their depth and configuration could lead to exposure to the stainless steel surface of the underlying substrate.
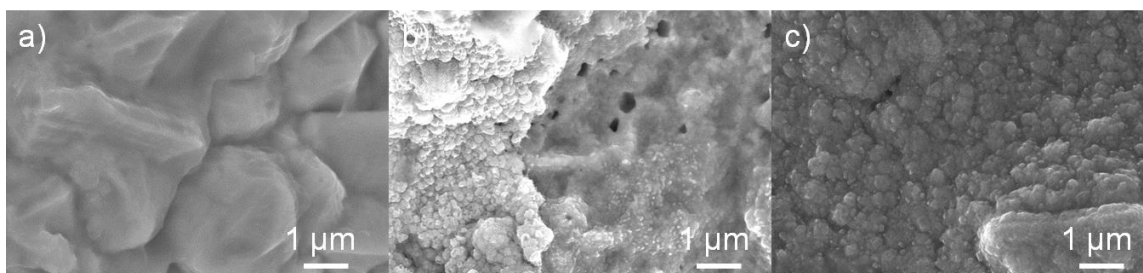

Figure 12. SEM images of catalysts electrodeposited using waveform "Pulsed L:" Samples (a) #13F (as-plated), (b) #15B (activated at 300 °C), and (c) #13E (activated at 350 °C).

Conclusions

Pulse-reverse methods were used to electrodeposit Cu films on stainless steel substrates. As-deposited films and films activated by a thermal oxidation/electrochemical reduction protocol were investigated for their performance in the electrocatalytic reduction of carbon dioxide, as a function of the electrodeposition and activation parameters. The electrocatalytic behavior of the samples was tested in an electrolysis cell at various cathodic half-cell potentials, with gaseous hydrocarbon products assayed by inline sampling to a gas chromatograph. Appreciable benefits in terms of overall hydrocarbon selectivity versus hydrogen evolution and other undesirable side reactions were observed from the use of pulsed versus DC electrodeposition, and the use of the activation protocol resulting in a strong shift in the hydrocarbon product distribution from CH_4 to C_2H_4. Future studies will focus on tailoring parameters such as substrate pretreatment, electrodeposition parameters (electrical waveform, electrolyte composition, etc.), and

activation parameters to enhance selectivity and activity, and to maximize the durability of the produced catalyst films.

Acknowledgments

References

1. R. P. S. Chaplin and A. A. Wragg, *J. Appl. Electrochem.*, **33**, 1107 (2003).
2. Y. Hori, A. Murata and R. Takahashi, *J. Chem. Soc., Faraday Trans 1*, **85**, 2309 (1989).
3. S. Verma, B. Kim, H.-R. M. Jhong, S. Ma and P. J. A. Kenis, *ChemSusChem*, **9**, 1972 (2016).
4. Y. Hori, I. Takahashi, O. Koga and N. Hoshi, *J. Phys. Chem. B*, **106**, 15 (2002).
5. K. W. Frese Jr, in *Electrochemical and Electrocatalytic Reactions of Carbon Dioxide*, p. 145, Elsevier, Amsterdam (1993).
6. A. C. Mishra, A. K. Thakur and V. Srinivas, *J. Mater. Sci.*, **44**, 3520 (2009).
7. E. J. Taylor and J. J. Sun, U.S. Patent US8603315 B2, (2013).
8. E. J. Taylor, *J. Appl. Sur. Fin. 3 (4) 178-89 (2008).*
9. W. E. G. Hansal, G. Sandulache and S. Hansal, *Meeting Abstr.*, **MA2017-01**, 1191 (2017).
10. T. D. Hall, S. H. Vijapur, E. J. Taylor, M. Inman and M. Brady, *Meeting Abstr.*, **MA2017-01**, 1179 (2017).
11. E. J. Taylor, E. B. Anderson and N. R. K. Vilambi, *J. Electrochem. Soc.*, **139**, L45 (1992).
12. S. Sen, B. Skinn, T. Hall, M. Inman, E. J. Taylor and F. R. Brushett, *MRS Adv.*, **2**, 8, 451-458 (2017).
13. C. W. Li and M. W. Kanan, *J. Am. Chem. Soc.*, **134**, 7231 (2012).
14. K. P. Kuhl, E. R. Cave, D. N. Abram and T. F. Jaramillo, *Energy Environ. Sci.*, **5**, 7050 (2012).
15. S. Sen, D. Liu and G. T. R. Palmore, *ACS Cat.*, **4**, 3091 (2014).
16. L. Yang, J. T. Frith, N. Garcia-Araez and J. R. Owen, *Chem. Commun.*, **51**, 1705 (2015).
17. C. Kim, G. Lee, C. Rhee and M. Lee, *Nanoscale*, **7**, 6627 (2015).
18. M. S. Chandrasekar and M. Pushpavanam, *Electrochim. Acta*, **53**, 3313 (2008).
19. Y. Choi, M. Kim and S. C. Kwon, *Surf. Coat. Technol.*, **169–170**, 81 (2003).
20. S. E. Hadian and D. R. Gabe, *Surf. Coat. Technol.*, **122**, 118 (1999).
21. Y. Hori, R. Takahashi, Y. Yoshinami and A. Murata, *J. Phys. Chem. B*, **101**, 7075 (1997).
22. W. J. Durand, A. A. Peterson, F. Studt, F. Abild-Pedersen and J. K. Nørskov, *Surf. Sci.*, **605**, 1354 (2011).
23. W. Tang, A. A. Peterson, A. S. Varela, Z. P. Jovanov, L. Bech, W. J. Durand, S. Dahl, J. K. Norskov and I. Chorkendorff, *Phys. Chem. Chem. Phys.*, **14**, 76 (2012).
24. P. Lobaccaro, M. R. Singh, E. L. Clark, Y. Kwon, A. T. Bell and J. W. Ager, *Phys. Chem. Chem. Phys*, **18**, 26777 (2016).